Title

Centrifuge Model Tests of Liquefaction-Induced Downdrag on Piles in Uniform Liquefiable Deposits

Journal

Journal of Geotechnical and Geoenvironmental Engineering, 148(7)

ISSN

1090-0241

Authors

Sinha, Sumeet K
Ziotopoulou, Katerina
Kutter, Bruce L

Publication Date

2022-07-01

DOI

10.1061/(asce)gt.1943-5606.0002817

Peer reviewed

Centrifuge Model Tests of Liquefaction-Induced Downdrag on Piles in Uniform Liquefiable Deposits

Sumeet K. Sinha, A.M.ASCE[1]; Katerina Ziotopoulou, M.ASCE[2]; and Bruce L. Kutter, M.ASCE[3]

Abstract: Earthquake-induced soil liquefaction can cause settlement around piles, which can translate to negative skin friction and the development of drag load and settlement of the piles. A series of centrifuge model tests were performed to assess liquefaction-induced downdrag and understand the interplay and effects of (1) pile embedment and pile-head load, (2) excess pore pressure generation and dissipation, and (3) reconsolidation and ground settlement on pile response during and postshaking. The model included a layered soil profile (clay, liquefiable sand, and dense sand) with two 635-mm-diameter instrumented piles. One pile was placed with its tip at the bottom of the liquefiable deposit; the other pile was embedded five diameters into the dense sand layer. The model was shaken with multiple earthquake motions with their peak horizontal accelerations ranging from 0.025 to 0.4 g. For each shaking event, the drag load on the piles first decreased during shaking and then increased during reconsolidation, exceeding its preshaking value. With multiple shaking events, the net drag load on the piles increased. The maximum observed drag load was found equal to the drained interface shear strength calculated from the interface friction angle of $\delta = 30°$ and a lateral stress coefficient of $K = 1$. Larger drag loads and smaller settlements were observed for the pile embedded deep in the dense sand layer. Most of the pile settlements occurred during shaking; postshaking pile settlement was less than 2% of the pile's diameter. The mechanisms behind the development of liquefaction-induced drag load on piles and settlements are described. Select ramifications concerning the design of piles in liquefiable soils are also described. **DOI: 10.1061/(ASCE)GT.1943-5606.0002817.**

Author keywords: Downdrag; Drag load; Liquefaction; Piles; Drag load; Centrifuge test.

Introduction

Pile foundations are typically designed to transfer axial loads at the pile head to deeper layers through upward (positive) interface shear stress (skin friction) and end bearing resistance [Fig. 1(a)]. However, if a soil layer around the pile settles more than the pile does, downward (negative) interface shear stress (skin friction) can develop [Fig. 1(d)]. Among other causes, ground settlement may result from reconsolidation following the earthquake-induced liquefaction of a soil layer. The net downward force due to negative skin friction, also called drag load (Q_d), increases the axial load in a pile beyond the pile head load, Q_f [Fig. 1(f)]. Consequently, both the positive skin friction below the liquefied layer and the load at the pile tip increases, and the pile settles until enough resistance is mobilized and force equilibrium is reestablished. The pile settlement caused by the drag load is known as downdrag (Fellenius 2006). The depth at which the soil and the pile settle equally (i.e., their relative movement is zero) is known as the neutral plane [Fig. 1(e)]. Above the neutral plane, the soil settles more than the pile, and negative skin friction (drag load) develops; below the neutral plane, the pile settles more than the soil, and positive skin friction is mobilized (Fellenius 2006). The resulting load distribution from the said negative and positive skin friction developed along the pile is maximized at the neutral plane [Fig. 1(f)].

The majority of the challenges related to the phenomenon of liquefaction-induced downdrag of piles relate to the timing and depth distribution of pore pressure generation and dissipation and reconsolidation settlements (Rollins 2017). In terms of its effects on resistance, liquefaction in the vicinity of the pile shaft leads to reduction (or loss for full liquefaction) of skin friction, while the presence of high excess pore pressures in the vicinity of the pile tip leads to reduction of end bearing resistance and its stiffness, and result in large pile settlements [Fig. 1(b)]. Fellenius and Siegel (2008) used the unified pile design method (Fellenius 2004) to evaluate the influence of liquefaction on the overall axial behavior of piles:

- During shaking, if liquefaction and the associated postliquefaction reconsolidation settlement occur above the initial static neutral plane (i.e., the neutral plane that exists before liquefaction), there is a minor effect on the axial load distribution and settlement of the pile. However, suppose partial or complete liquefaction occurs below the initial static neutral plane. In that case, more loads will be transferred to the pile's shaft and tip below the liquefied layer, causing settlement of the pile.
- Postshaking, excess pore pressures dissipate, soil regains its shear strength, and postliquefaction reconsolidation strains lead to settlements in the liquefied layer and the layers above it, causing the development of negative skin friction and thus drag load on the pile. If postliquefaction settlement occurs below the initial static neutral plane, it shifts the neutral plane downward and increases drag load on the pile. Correspondingly, the increased drag load extra load is balanced by mobilizing larger positive skin friction and tip resistance with a further pile settlement [Fig. 1(c)].

[1]Graduate Student Researcher, Dept. of Civil and Environmental Engineering, Univ. of California, Davis, One Shields Ave., Davis, CA 95616 (corresponding author). ORCID: https://orcid.org/0000-0002-2011-4887. Email: skssinha@ucdavis.edu

[2]Assistant Professor, Dept. of Civil and Environmental Engineering, Univ. of California, Davis, One Shields Ave., Davis, CA 95616. Email: kziotopoulou@ucdavis.edu

[3]Professor Emeritus, Dept. of Civil and Environmental Engineering, Univ. of California, Davis, One Shields Ave., Davis, CA 95616. ORCID: https://orcid.org/0000-0002-0628-1275. Email: blkutter@ucdavis.edu

Note. This manuscript was submitted on June 1, 2021; approved on February 23, 2022; published online on April 27, 2022. Discussion period open until September 27, 2022; separate discussions must be submitted for individual papers. This paper is part of the ***Journal of Geotechnical and Geoenvironmental Engineering***, © ASCE, ISSN 1090-0241.

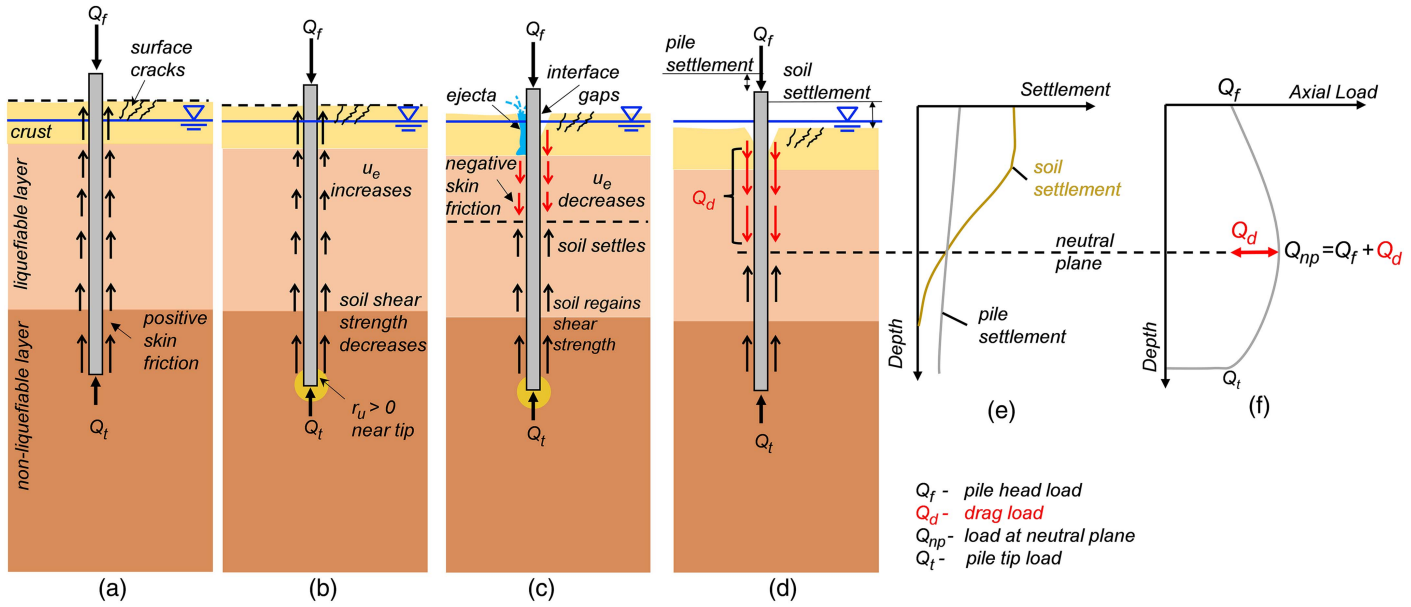

Fig. 1. Illustration of the development of liquefaction-induced downdrag on piles: Mechanism of shear stress distribution, soil and pile settlement, and tip resistance: (a) before shaking; (b) during shaking; (c) during reconsolidation; (d) at the end of reconsolidation showing (e) soil and pile settlement profile; and (f) axial load distribution in piles.

If it occurs above the initial static neutral plane, the increase in the drag load and settlement of the pile is small.

While these mechanisms presented are reasonable based on our current understanding, the overall timing between the rate of excess pore pressure generation/dissipation and soil settlement can affect the development of downdrag and drag loads. If most of the soil settlement occurs when effective stresses are low, the developed negative skin friction and, thus, the drag are smaller compared to a case with higher effective stresses. A small amount of soil settlement toward the end of reconsolidation (when effective stresses are high) might be enough to mobilize full negative skin friction in the reconsolidated soil. Sinha et al. (2019) performed multiple t-z spring simulations to study the effect of reconsolidation settlements and pile tip conditions on liquefaction-induced downdrag on piles. The study found that the downdrag settlement and drag load increased with reconsolidation settlements occurring deeper in the soil layers and around the pile's tip. End bearing piles developed larger drag loads than the floating piles; however, the resulting downdrag settlement was smaller. Coelho et al. (2004) performed dynamic centrifuge tests on uniform deposits of saturated sands and showed that the mechanisms of excess pore pressure generation and liquefaction are similar in dense and loose sand, with the rate of excess pore pressure generation being slower in dense sand. Centrifuge tests of pile groups by Knappett and Madabhushi (2009) and Stringer and Madabhushi (2010, 2013) observed substantial settlements of piles during shaking when the excess pore pressures were high around the shaft and near the tip. After shaking, as soil reconsolidated and drag load developed, the resulting settlement in the piles was much smaller.

The hydraulic boundary conditions can also significantly affect the overall response of the soil–pile system: the presence of cracks and interface gaps, if they develop around the pile [Fig. 1(c)], can speed up reconsolidation and influence the downdrag phenomenon. Interface gaps essentially result in zero shaft resistance and provide a hydraulic exit to the fluid resulting in ejecta at the surface. The movement of the fluid through interface gaps can erode the soil and further reduce the drag loads. Interbedded soil deposits can bring additional complexities due to entrapment and slow dissipation of excess pore pressures within the low permeable layers.

Estimating the drag load for pile design requires estimating the mobilized negative skin friction on the pile in the liquefiable and nonliquefiable layers above the neutral plane. Downdrag is then estimated as the pile settlement needed to mobilize the positive skin friction and tip resistance that balance the drag load. The current state of practice follows recommendations from AASHTO (2020) as well as findings from other advanced research in this field (e.g., Boulanger and Brandenberg 2004; Rollins and Strand 2007; Fellenius and Siegel 2008; Hannigan et al. 2016; Muhunthan et al. 2017). AASHTO (2020), in particular, uses a criterion on soil settlement or the neutral plane solution approach to determine the location of the neutral plane and the associated drag load. The general approach assumes negative skin friction (above the neutral plane) equal to a residual soil strength in the liquefiable zone and nonliquefied skin friction in the nonliquefiable layers above the liquefaction zone. AASHTO (2020) also requires combining drag loads with all other seismic loads (e.g., inertial loads from the superstructure) and does not account for the aforementioned timing of the various mechanisms. Boulanger and Brandenberg (2004) modified the neutral plane method to account for the timing of the soil settlement with the dissipation of excess pore pressures during reconsolidation. In their method, Boulanger and Brandenberg (2004) assumed mobilization of interface shaft friction as a linear function of excess pore pressure ratio ($1 - r_u$). Through blast-induced liquefaction tests performed on driven piles, Rollins and Strand (2006) recommended that the negative skin friction in the fully reconsolidated layer be taken as approximately 50% of the mobilized positive skin friction before liquefaction. Other blast-induced liquefaction studies conducted on auger-cast piles (Rollins and Hollenbaugh 2015; Nicks 2017) and micro piles (Rollins et al. 2019; Lusvardi 2020) observed similar results. While these recommendations are consistent, there have been cases within these studies (Rollins and Strand 2007; Strand 2008; Rollins and Hollenbaugh 2015; Elvis 2018) where the developed negative skin friction in the reconsolidated layer was greater than 50% of the positive skin friction before

liquefaction. For sites with earthquake drains installed, Rollins and Strand (2007) observed the development of negative skin friction equal to 100% of the mobilized positive skin friction before liquefaction. Blast-induced liquefaction studies by Elvis (2018) on driven steel piles and drilled piles found the mobilized negative skin friction, respectively, to be 50%–75% and 75%–90%, of the positive skin friction before liquefaction. Fellenius and Siegel (2008) used a zero negative skin friction in the fully liquefied zone to estimate liquefaction-induced drag load. Vijayaruban et al. (2015), Muhunthan et al. (2017), and Fellenius et al. (2020) used the neutral plane method with zero negative skin friction in the fully liquefied zone for studying the liquefaction-induced downdrag for the Juan Pablo II bridge at the 2010 Maule Earthquake in Chile. They found that the settlement caused by the downdrag was relatively small and that the cause of failure was liquefaction of the soil below the pile tip. The Federal Highway Administration (FHWA) (Hannigan et al. 2016) recommend the use of neutral plane methods with soil behavior models (t-z and q-z models) calibrated from field tests to determine the drag load. The studies discussed provide no clear resolution regarding the magnitude of negative skin friction at the interface and do not consider that the neutral plane shifts during reconsolidation.

In the present study, a series of centrifuge tests were performed to investigate the factors affecting the magnitude of liquefaction-induced drag loads of piles and the settlements experienced in the soil and the pile. The centrifuge model test included two piles with a diameter of 635 mm passing through a thick liquefiable layer, embedded at different depths within an underlying deeper dense layer. The piles were heavily instrumented to monitor the axial load distribution, enabling the assessment of the skin friction distribution along the length of the pile. The model was shaken with a sequence of realistic earthquake motions with different intensities. The effects of excess pore pressure generation/dissipation, soil settlement, pile tip embedment, and pile head load on liquefaction-induced downdrag are studied. Finally, future work and implications for the design of axially loaded piles in liquefiable soils are summarized.

Centrifuge Model

A centrifuge model test SKS02 (Sinha et al. 2021) was performed on the large 9-m-radius centrifuge at the University of California, Davis. The test was performed at a centrifugal acceleration of 40 g. All numerical quantities presented in this paper have been converted to prototype units according to the scaling laws described by Garnier et al. (2007) unless explicitly mentioned otherwise.

The test was performed in a flexible shear beam container (FSB2) consisting of a rigid base plate and five rings, with internal dimensions of $1.651 \times 0.787 \times 0.553$ m in length, width, and depth, respectively. The container rings were sandwiched with soft rubber interfaces providing lateral flexibility. Vertical shear rods were placed on both the north and south ends of the container to provide complementary shear stresses. Ilankatharan (2008) describes this container in more detail.

The model represented a layered soil profile of a 9-m-thick loose liquefiable Ottawa F-65 sand ($D_R \approx 42\%$–44%) layer sandwiched between 4 m of an overconsolidated coarse kaolin clay layer ($\sigma'_p = 100$ kPa) at the top and an 8-m-thick dense Ottawa F-65 sand layer ($D_R \approx 86\%$–88%) (Fig. 2). Table 1 summarizes the thicknesses, relative densities, and total densities of the constructed soil profile. Using the minimum and maximum density procedures developed as part of the Liquefaction Experiments and Analyses Project (LEAP) (Carey et al. 2020), several tests were performed to measure the mean grain size diameter (D_{50}), the maximum and minimum void ratios ($e_{\max}$ and $e_{\min}$), and the grain size distribution for the Ottawa F-65 batch used in the test. The index properties of all the soils used in the test are provided in Table 2. The critical state friction angle (ϕ'_{cv}) of Ottawa F-65 soil is approximately 30° (Bastidas 2016).

The model was built in stages. First, the dense and loose sand layers were constructed using the dry pluviation method to achieve the target relative densities of $D_R \approx 88\%$ and $D_R \approx 42\%$, respectively. The pore fluid for the sands consisted of a deaired 2% mixture of methyl-cellulose and deionized water solution having a viscosity of approximately 25 times that of pure water. The viscosity was selected to be large enough to ensure that the duration of pore pressure dissipation would be significantly greater than the duration of shaking but low enough to allow saturation in a reasonable time frame. For saturation, the model container was covered with a vacuum lid followed by applying three cycles of a vacuum of 98 kPa and then flushed with carbon dioxide to remove at least 99% of the air entrapped in the soil pores. The container was then tilted

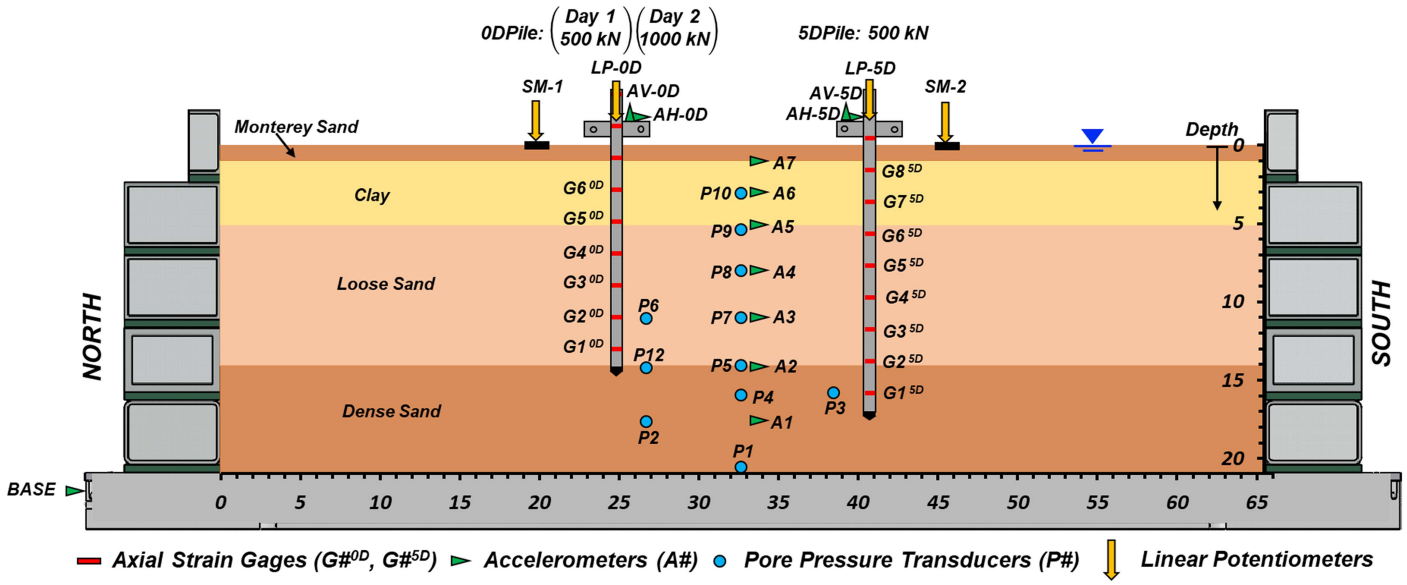

Fig. 2. Cross-sectional view of the centrifuge model test.

J. Geotech. Geoenviron. Eng., 2022, 148(7): 04022048

Table 1. Soil layer properties

Soil layer	Relative density[a] D_R (%)	Thickness (m)	Saturated density (kg/m^3)
Monterey sand	95	1	2,054
Clay layer	—	4	1,713
Loose sand	42–44	9	1,968
Dense sand	86–88	7.2	2,060

[a]Measured during model construction.

Table 2. Index properties of soils used in the centrifuge test

Properties	Ottawa F-65 sand	Monterey sand	Coarse Kaolin clay
Specific gravity, G_s	2.65[a]	2.64[a]	2.58[b]
Grain size, D_{50}	0.2 mm[a]	0.95 mm[a]	4 μm[b]
Minimum void ratio, e_{min}	0.52[a]	0.536[a]	—
Maximum void ratio, e_{max}	0.83[a]	0.843[a]	—
Liquid limit (LL)	—	—	46.8%[b]
Plasticity index (PI)	—	—	18.5%[b]
USCS	SP	SP	ML

[a]Sinha et al. (2021).
[b]Stringer et al. (2013).

at an angle of 2°. With vacuum applied, the deaired 2% methyl-cellulose solution was slowly introduced in the model to make a small pool of solution on the sand surface at the lower end of the tilted container. As soil saturated and the wetting front progressed across the model's surface, the depth of the pool was increased until the model was fully submerged. When saturation was completed, the vacuum was slowly released, the vacuum lid was removed, and the box was leveled (Sinha et al. 2021). The clay layer was placed using a slurry deposition method. The slurry consisted of a coarse Kaolin clay mixture with a water content of $w = 80\%$ mixed under a vacuum of 45 kPa. The slurry was placed in the model and then consolidated to vertical stress of 100 kPa using a hydraulic press. Consolidation was performed slowly in stages with a loading increment of 3.4 kPa. A high overconsolidation ratio (OCR) of about 10 at the top and about 4 in the middle of the clay layer was targeted to maximize the drag load developed in the piles such that it would be measurable in the centrifuge test. On average, and based on the hand vane shear test (VST_6) performed at the beginning of the test later, the clay layer had an undrained shear strength of $s_u = 22$ kPa (Table 3). A 1-m-thick relatively permeable coarse-grained Monterey sand layer was dry pluviated on the top of the clay layer and saturated with deaired 2% methyl-cellulose solution. The primary function of the Monterey sand was to provide known vertical stress on the top of the clay layer and preclude desiccation of the clay layer from the dry wind of the centrifuge spinning at 64 rpm.

The model was transported to the centrifuge arm on a forklift following model preparation and saturation. To prevent the densification of the saturated model from the vibrations generated during transport, the model was covered with a membrane and transported while subjected to a confining pressure of 40 kPa maintained using a vacuum pump (Sinha et al. 2021).

Pile Properties, Instrumentation, and Installation

The experiment included two 1/40 scale models of aluminum closed-ended piles with an outer diameter (D) of 635 mm and an inner diameter of 564 mm. For obtaining maximum drag load, the outer surface of the pile was machined to achieve an average roughness (R_a) of 0.04 to 0.06 mm. The achieved interface profile is shown in Fig. 3(c). According to Martinez and Frost (2017), this roughness was sufficient to mobilize the interface friction angle (δ) equal to the drained soil friction angle of $\phi'_{cv} = 30°$ [Fig. 3(d)].

The pile was instrumented internally to measure the axial load distribution. While instrumenting the outer surface would be easier, it would be challenging to secure the sensor wires while achieving a uniform diameter and roughness profile. With the instrumentation inside, the strain gauges and their wires were secured from abrasion, making the pile reusable for multiple tests. Nine strain gauge bridges were installed with a spacing of about 2 m (i.e., about 5.08 cm at model scale) [Fig. 3(a)]. For each pile, the gauges were labeled 1 to 9 from bottom to top [Fig. 3(a)]. The bottommost gauge in the piles was placed at about 1.27 m (i.e., 3.175 cm at model scale) from its tip [Fig. 3(a)]. Although the strain gauges were wired in a full-bridge configuration to measure axial load, the bridges had some sensitivity to bending moments. Two-point bending moment tests on different loading axes were conducted on the piles to determine the orientation corresponding to the minimum cross-axis sensitivity. During the test, the piles were oriented about those axes to minimize the error in axial load measurements arising from the bending moments generated during shaking. The fully assembled pile is shown in Fig. 3(b). The bottom of the pile was plugged with an O-ring sealed tip [Fig. 3(b)], to keep the sensors safe from water seeping from the bottom. The apex angle of the tip was designed to be 120° to facilitate pile installation. A split mass mechanism was clamped to attach the desired mass to the pile with its center of mass 1 m above the soil surface.

The piles were pushed in at 1 g by using a crane to lower a heavy mass onto the top of the pile. One pile referred to as the "5DPile"

Table 3. Testing sequence

Event	Description	Measurements
	Day 1	
VST_6	Hand vane shear test	$s_u = 22$ kPa[a]
PLT_1	Pile load test	Fig. 5(a)
$VST_7 - VST_8$	Hand vane shear test	$s_u = 22$ kPa[a]
	Spin-Up 1	
CPT_1	Cone penetration test	Fig. 5(a)
EQM_1	Small Santa Cruz	PBA = 0.026 g
EQM_2	Medium Santa Cruz	PBA = 0.14 g
CPT_2	Cone penetration test	Fig. 5(a)
EQM_3	Large Santa Cruz	PBA = 0.24 g
	Spin-down	
$VST_9 - VST_{10}$	Hand vane shear test	$s_u = 25$ kPa[a]
	Day 2	
PLT_2[b]	Pile load test	Fig. 5(a)
VST_{11}[b]	Hand vane shear test	$s_u = 25$ kPa[a]
	Spin-Up 2	
CPT_3[b]	Cone penetration test	Fig. 5(a)
EQM_4[b]	Medium Santa Cruz	PBA = 0.14 g
EQM_5[b]	Large Santa Cruz	PBA = 0.32 g
CPT_5[b]	Cone penetration test	Fig. 5(a)
EQM_6[b]	Large EJM01[c] motion	PBA = 0.40 g
	Spin-Up 3	
VST_{12}[b] - VST_{13}[b]	Hand vane shear test	$s_u = 37$ kPa[a]

Note: Peak base acceleration (PBA) measured at the bottom of the container.
[a]Peak undrained shear strength (su) measured at the middle of the clay layer (Sinha et al. 2021).
[b]Load on 0DPile was increased from 500 to 1,000 kN.
[c]Malvick et al. (2002).

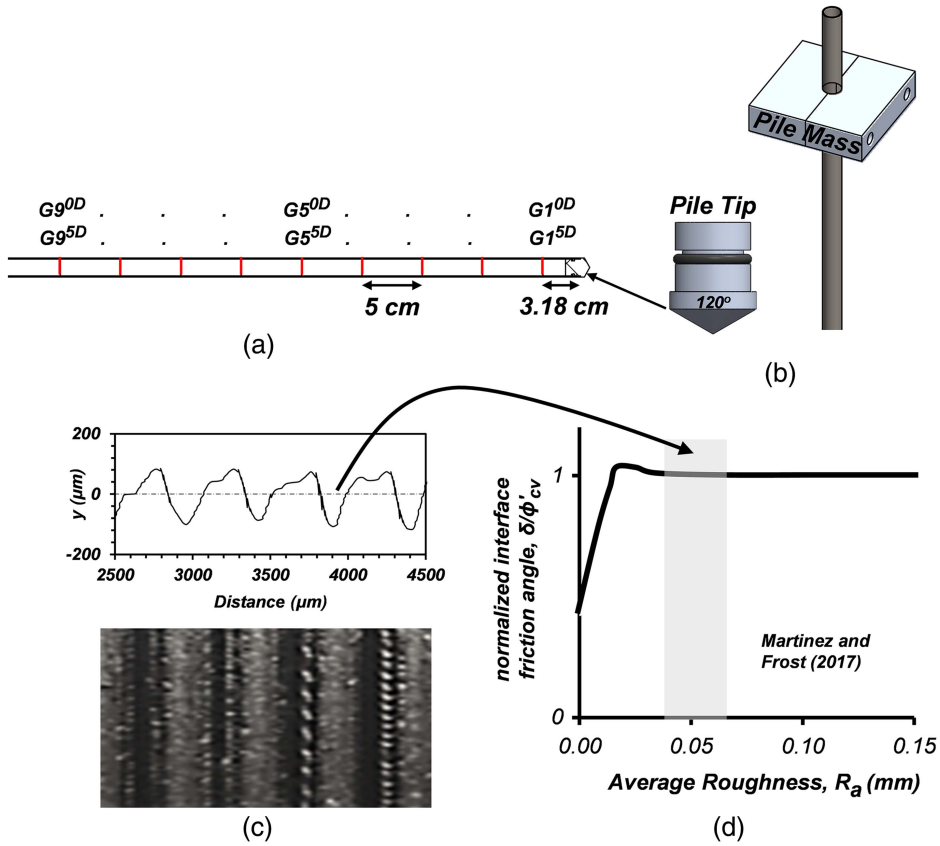

Fig. 3. Instrumented model pile: (a) with nine internally installed full-bridge axial strain gauges; (b) model pile mass and pile tip apex angle of 120°; and (c) machined average interface roughness (R_a) of 0.04–0.06 mm enough to mobilize the (d) interface friction angle (δ) equal to the drained soil friction angle (ϕ'_{cv}).

was embedded until its tip was 5 diameters into the dense sand. The "0DPile" tip was placed at the top of the dense sand.

Model Instrumentation

The model was instrumented with accelerometers (As), pore pressure transducers (Ps), linear potentiometers (LPs), and settlement markers (SMs) (Fig. 2). The linear potentiometers (SM-1, SM-2) and (LP-0D, LP-5D) were used to measure soil and pile settlements, respectively. The axial strain gauges in 0D and 5DPiles were numbered as $G1^{0D}$–$G9^{0D}$ and $G1^{5D}$–$G9^{5D}$ starting from the pile's tip to its head [Fig. 3(a)]. Accelerometers: AH-0D, AV-0D, AH-5D, and AV-5D installed on the pile head mass were used to measure horizontal and vertical accelerations of 0D and 5DPiles. An accelerometer (BASE) was attached at the base of the container to measure the applied shaking.

Tracking the State of the Model

Cone penetration tests (CPTs), pile load tests (PLTs), and vane shear tests (VSTs) were performed to determine the state of the model at different phases of the test. The cone penetration test was performed using a 6-mm-diameter (model scale) cone with an apex angle of 60°. The CPT probe had a load cell attached to the tip, which measured the tip stress as it penetrated the soil. The stroke of the CPT characterized soil up to the depth of 12 m (prototype scale). For characterizing the deeper soil layers, a PLT was designed, where a 10-mm-diameter (model scale) solid steel pile with an apex angle of 120° (same as the instrumented pile) was pushed with the help of a hydraulic actuator to a depth of 18 m (prototype scale). The PLT probe was initially embedded at 1 g to the depth of 12 m and then pushed to 18 m while in flight at 40 g. The only instrumentation in the PLT probe was an external load cell attached to its head that measured the total pile load (skin friction and end bearing) as it penetrated the soil. Hand vane shear tests using a 33-mm (model scale) blade were used to measure the undrained shear strength of the clay layer between spins.

Testing Sequence

Testing was performed over 2 days, and the test sequence is shown in Table 3. On the first day of testing, the dead load on both the piles was 500 kN. On the second day, the load on the 0DPile was increased to 1,000 kN. With the piles installed, the model was spun up to 40 g and shaken with multiple small (EQM_1), medium (EQM_2, EQM_4), and large (EQM_3, EQM_5, EQM_6) scaled Santa Cruz earthquake motions with peak base accelerations (PBA) ranging from 0.025 to 0.4 g [Figs. 4(a–c)]. EQM_6 was a long-duration, strong Santa Cruz motion followed by five small magnitude Santa Cruz motions. CPTs and PLTs were performed while spinning the model at 40 g; the VSTs were measured by hand at 1 g after spinning down the centrifuge. Enough time was allowed between each shaking event to completely dissipate the excess pore pressures from all the layers. Dissipating excess pore pressures from the clay layer took the longest time. For medium shaking events (EQM_2, EQM_4), it took about 3 hours (4.5-min model scale) to completely dissipate (i.e., greater than 90%) the excess pore pressures in the clay layer. For strong shaking events (EQM_3, EQM_5, EQM_6), complete dissipation took up to 5 hours (7.5-min model scale).

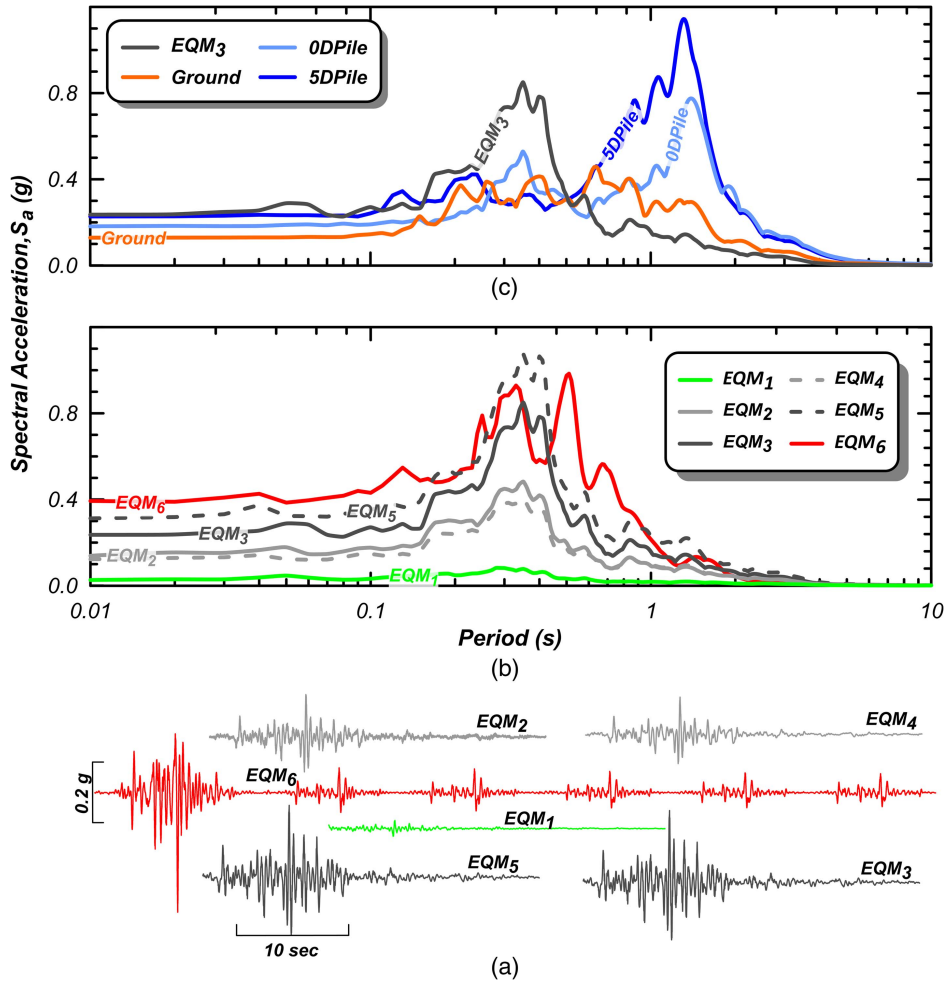

Fig. 4. Earthquake motions of the centrifuge model test: (a) spectral accelerations recorded for input motion (EQM_3) at the base of the model, the model surface, and the 0DPile and 5Dpile; (b) spectral accelerations of applied earthquake motions; and (c) time histories of applied earthquake motions.

Model Test Results

The time histories of the applied earthquake motions and their response spectra are shown in Figs. 4(a–c). For shaking event EQM_3, the spectral acceleration of the applied input motion at the base of the model, at the soil surface, at the 0DPile mass, and at the 5DPile mass are also shown in Figs. 4(a–c). The spectra show that the input motions had a predominant period between 0.3 and 0.4 s [Fig. 4(b)] and the piles' first fundamental period was between 1.2 and 1.4 s [Fig. 4(a)]. The predominant period of the motions was designed to be away from the first fundamental period of the piles to ensure that the piles would not undergo strong horizontal movements generating large moments, which might affect the accuracy of the axial load measurements.

Cone tip resistance (q_c), relative density (D_R), and soil shear strength interpreted from CPTs, PLTs, and VSTs for different shaking events are shown in Figs. 5(a–d). Sinha et al. (2021) describe the details on processing the CPT data. The external load cell results obtained from the pile load test were corrected for the cone tip apex angle and skin friction effect to obtain the cone tip resistance (q_c) in the dense layer (Sinha et al. 2021). Hand vane shear tests along with the measured water content at 1 g were used to obtain the undrained shear strength (s_u) profile in the clay layer (Sinha et al. 2021) [Fig. 5(d)]. PLT_1, CPT_1, and VST_6–VST_8 were conducted before EQM_1 to measure the model's initial (preshaking) state. The D_R of the sand layer interpreted from the CPT and PLT matched quite well with the pluviated D_R's (i.e., about $D_R \approx 44\%$–46% in the loose sand layer and $D_R \approx 90\%$ in the dense sand layer). The undrained shear strength in the middle of the clay layer was estimated to be about $s_u = 22$ kPa. After shaking the model with a medium (EQM_2) and a large (EQM_3) earthquake motion, the liquefaction-induced settlement increased D_R in the loose sand layer to $D_R \approx 49\%$. The undrained shear strength in the clay layer increased to $s_u \approx 25$ kPa. The increase of the undrained shear strength of the clay layer resulted from the consolidation strains induced from shaking. On the second day and after the two large shaking events, EQM_5 and EQM_6, the D_R in the loose sand increased to $D_R \approx 58\%$, whereas the undrained shear strength in the clay layer increased to $s_u = 37$ kPa. The drained interface shear strength in the liquefiable (loose) sand layer is shown in Fig. 5(d), assuming a lateral stress coefficient, $K = 1$ [as for a driven cast in situ pile (Fleming et al. 2008)] with an interface friction angle of $\delta = 30°$. Here, K is defined as the ratio of effective radial stress at the pile's interface to effective vertical stress. The shear strength presented in Fig. 5(d) was later used to estimate the shaft resistance and calculate the limit load curve for the piles. The mechanism of liquefaction-induced downdrag is described ahead in reference to Figs. 5–10.

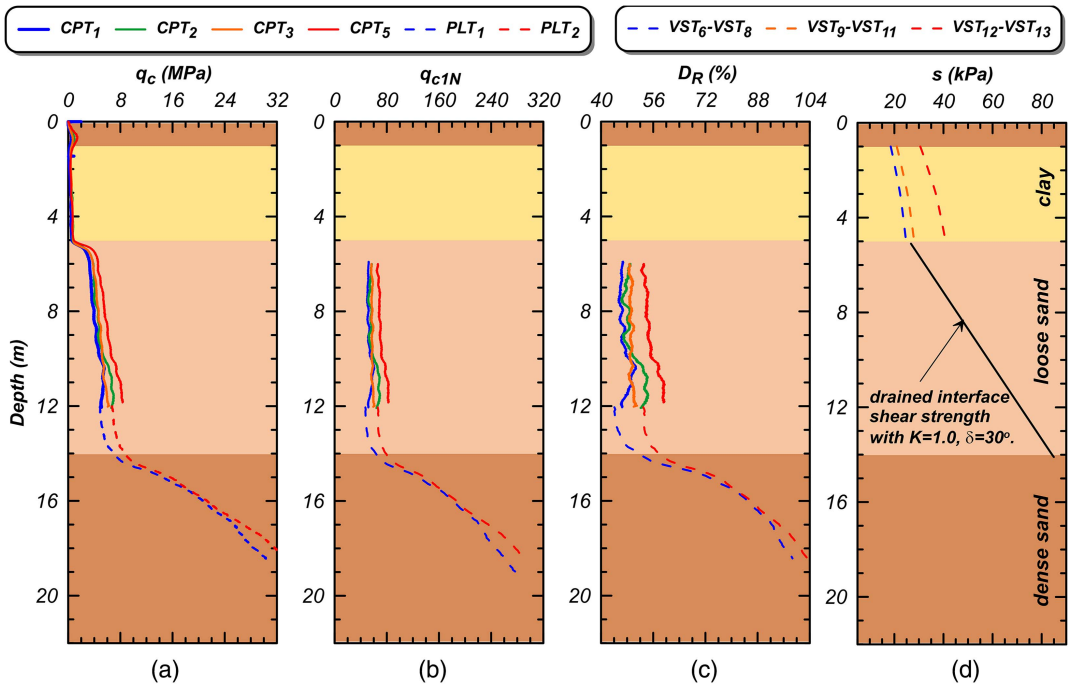

Fig. 5. (a) Cone tip resistance (q_c); (b) normalized overburden corrected cone tip resistance (q_{c1N}); (c) relative density (D_R); and (d) and shear strength (s) interpreted from CPTs, PLTs, and VSTs performed at various times (see Table 3) during the centrifuge test.

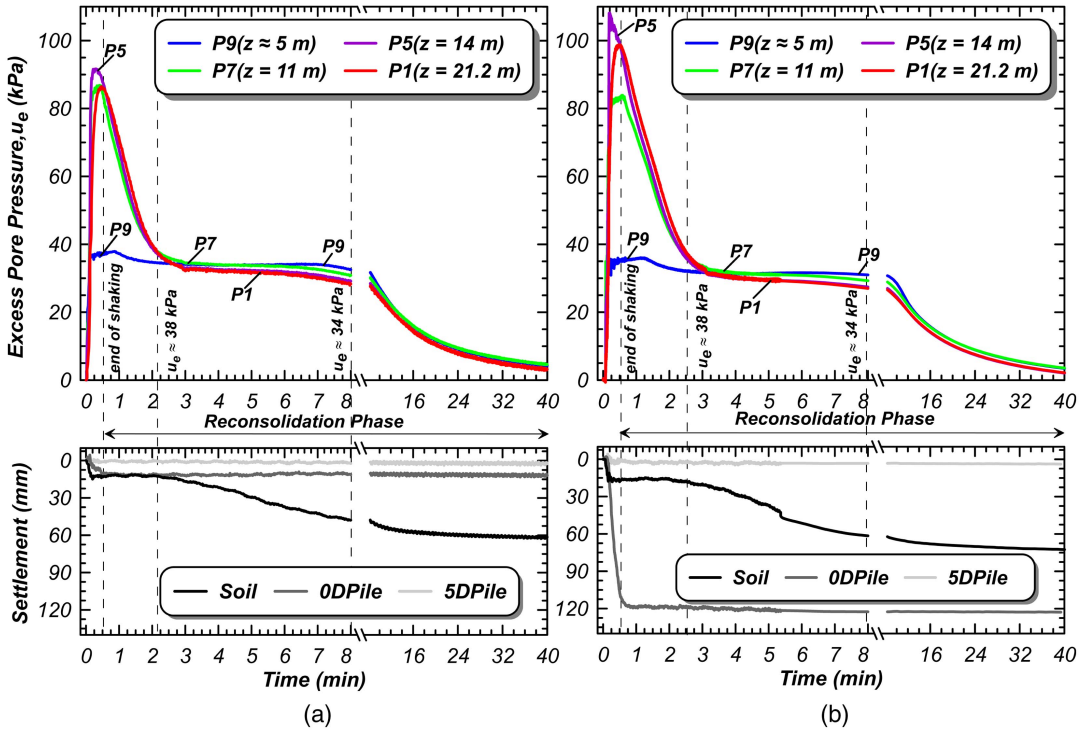

Fig. 6. Excess pore pressure time histories and soil and pile settlement time histories for shaking events: (a) EQM_3 (on day 1); and (b) EQM_5 (on day 2).

Centrifuge Spin-Up–Induced Drag Load

The spinning up of the centrifuge resulted in drag loads (as subsequently shown in Fig. 10). As the centrifuge spun up, the increase of gravity resulted in the development of u_e in soil (measured at the pore pressure transducers). These excess pore pressures dissipated after reaching the target centrifugal acceleration of 40 g. The dissipation of these pore pressures resulted in soil consolidation settlements and hence negative skin friction and drag load on the pile. At the end of centrifuge spin-up, the 0DPile and the 5DPile developed drag loads of about 250 kN and 700 kN, respectively

J. Geotech. Geoenviron. Eng., 2022, 148(7): 04022048

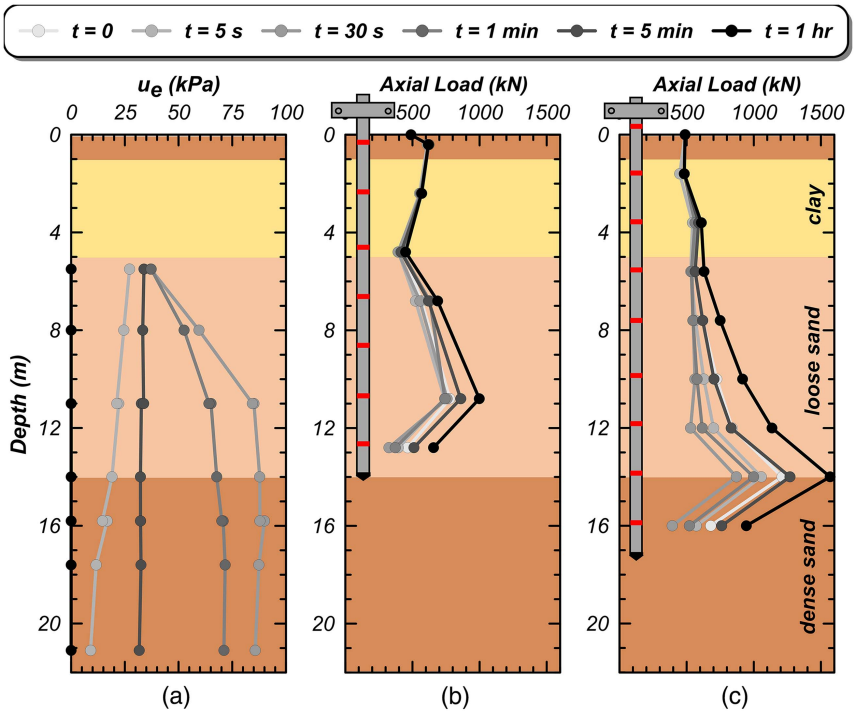

Fig. 7. Development of liquefaction-induced downdrag on piles. Isochrones of (a) excess pore pressure profile and axial load distribution for: (b) 0DPile; and (c) 5DPile for shaking event EQM_3.

(as subsequently shown in Fig. 9). Their initial static neutral planes were about 11 m and 14 m deep, respectively. The consolidation settlement from centrifuge spin-up that caused the development of drag loads could not be precisely measured. The consolidation of the clay layer and the unknown settlement of the racks connected to the settlement sensors under increasing gravity made it difficult to obtain settlements precisely. The soil settlement during spin-up one was qualitatively estimated (using the stiffness of the racks and the clay layer calibrated from multiple spin-up and spin-down measurements) to be about 20–30 mm in the sand layers and about 10–15 mm in piles.

Liquefaction-Induced Drag Load

During several shaking events: EQM_3, EQM_5, and EQM_6, liquefaction occurred in portions of the loose and medium dense sand layers. Significant excess pore pressures were also measured in the dense sand layer. On the other hand, there were shaking events: EQM_2 and EQM_4, which did not cause liquefaction but did produce measurable small excess pore pressures. However, the dissipation of these small excess pore pressures and reconsolidation caused enough soil settlement to cause drag loads and downdrag settlements of the piles. Figs. 6(a and b) illustrate u_e time histories at four select pore pressure transducers and soil and pile settlement time histories for shaking events EQM_3 and EQM_5. Figs. 7(a–c) show u_e isochrones in the soil [Fig. 7(a)] and axial load distribution in 0DPile [Fig. 7(b)] and 5DPile [Fig. 7(c)] for shaking event EQM_3. During shaking event EQM_3, the top 7 m of the loose sand layer (i.e., between depths 5–12 m) liquefied. The mobilized interface shear stress, the mobilized pile tip stress, and the soil and pile settlement in response to an excess pore pressure ratio (r_u) in the liquefied layer and near the pile's tip for shaking event EQM_3 are shown in Figs. 8(a–d). Soil and pile settlement at the end of shaking ($t = 30$ s), during reconsolidation ($t = 2.5$ min), and after complete reconsolidation are summarized in Table 4 for all the shaking events (EQM_1–EQM_6). The soil settlement shown in the plots and the tables were taken as the average of settlements measured from the two settlement sensors, SM-1 and SM-2. The mechanisms observed during and postshaking were the same across all large shaking events and are thus only described in this paper in reference to shaking event EQM_3. Please note that the data for all other shakings are provided in Sinha et al. (2021). In what follows, some of the mechanisms are described in reference to Figs. 7 and 8.

During Shaking

At the beginning of shaking ($t = 0$ s), the piles had an initial drag load, and correspondingly an initial static neutral plane developed from the negative skin friction either from centrifuge spin-up or previous shaking events [Figs. 7(b and c)]. For the shaking event EQM_3 ($t = 0$ s), the piles had an initial drag load developed from previous shaking events EQM_1 and EQM_2. At the beginning of the shaking (i.e., even before soil started developing excess pore pressures), a small reduction of negative skin friction [Fig. 8(c)] and a compensating increase in the mobilized pile tip stress [Fig. 8(d)] occurred. This initial decrease in skin friction could have resulted from the relaxation of shear stresses from the disturbance caused by the shaking. At the beginning of the shaking, some soil (surface) settlements occurred in the models [Figs. 6(a and b), Table 4]. The initial surface settlement could have resulted from the undrained movement of the soil caused by the tendency of flat ground surface conforming to the curved g-field in the centrifuge.

Excess pore pressures generated in the soil layers during shaking decreased skin friction, decreasing drag loads, and thus axial loads in the piles. At $t = 5$ s, excess pore pressures in soil started to develop. As a result, the negative skin friction and drag loads [Fig. 8(c)] decreased. In addition, the r_u build-up and strength loss throughout the model [Figs. 6 and 7(a)] also decreased positive skin friction and the tip resistance below the initial static neutral plane. The decrease in drag load caused a decrease in axial loads in the piles [Figs. 7(a and b)]. Typically, the decrease in drag load

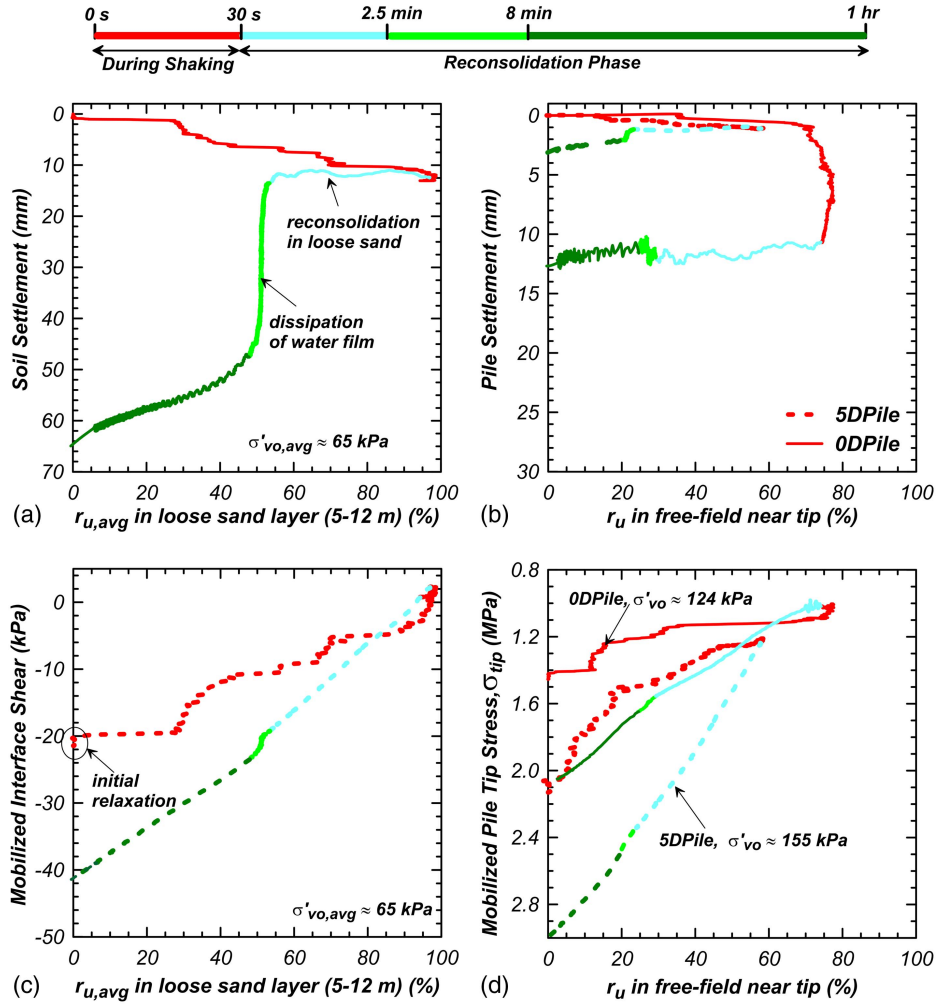

Fig. 8. Development of: (a) soil; (b) pile settlement; (c) average mobilized interface shear stress in the loose sand layer (5–12 m); and (d) mobilized pile tip stress as excess pore pressures changed in soil layers during the shaking event EQM_3. Shaking ended at ($t = 30$ s), equalization of excess pore pressures ($u_e \approx 38$ kPa) was first achieved at $t \approx 2.5$ min, the water film beneath the clay layer disappeared at $t \approx 8$ min, and complete reconsolidation (>98%) was achieved at about $t = 1$ h.

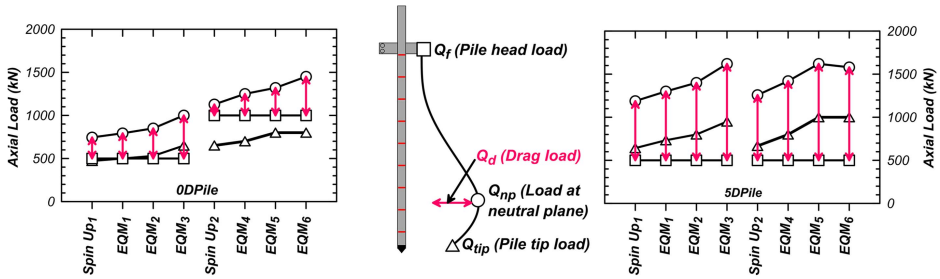

Fig. 9. Summary of pile head load (Q_f), developed drag load (Q_d), and pile tip load (Q_{tip}) after consolidation due to centrifuge Spin-Up (1 and 2) and shaking events EQM_1–EQM_6.

surpassed the decrease in shaft resistance below the neutral plane resulting in a decrease in pile tip stress [Fig. 8(d)].

When the soil liquefied, the drag load was reduced to zero, and high excess pore pressures were generated in the dense sand layer. At the peak of shaking, the loose sand layer liquefied between the depths of 5 and 12 m while generating high excess pore pressures of $u_e \approx 80$ kPa were achieved in the dense sand layer [Fig. 7(a)]. While the dense sand is expected to exhibit small earthquake-induced excess pore pressures, water migration from the loose sand layer to the dense layer resulted in increased excess pore pressures. The magnitude of pore pressure increase in the dense layer depends on the relative thicknesses of the layers and drainage boundary conditions. This issue is examined in more detail in Sinha (2022). When the loose sand layer was fully liquefied (between the depths of 5–12 m), the interface skin friction for the 5DPile in the liquefied layer was reduced to zero and, consequently, the drag load vanished

J. Geotech. Geoenviron. Eng., 2022, 148(7): 04022048

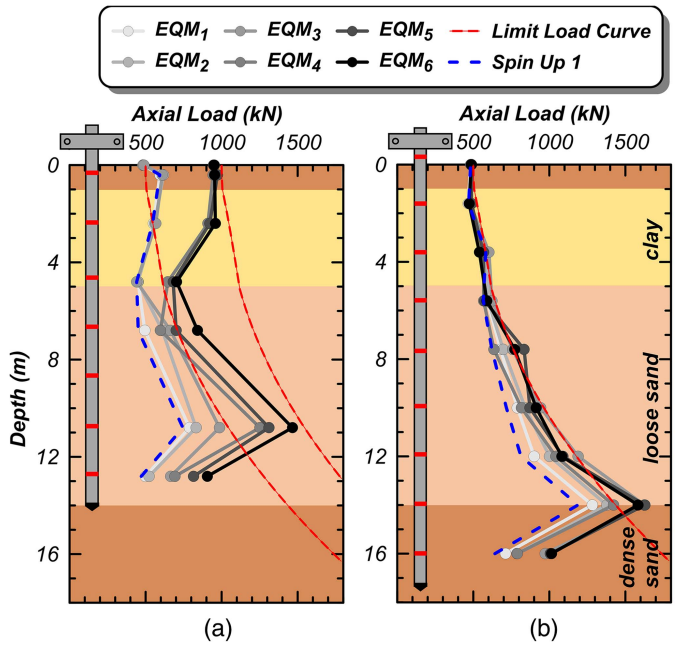

Fig. 10. Axial load distribution at the end of consolidation from Spin-Up 1 and shaking events EQM_1–EQM_6 in: (a) 0DPile; and (b) 5DPile.

[Fig. 8(c)]. Similar observations were made for the 0DPile; however, due to the aforementioned cross-sensitivity in the axial gauges, the interface skin friction (obtained from axial gauge measurements) did not reduce to zero. During the posttesting model dissection, the 0DPile was found inclined vertically by about 1.4° in the shaking direction. Thus, inclination might have introduced residual moments in the 0DPile affecting the axial load measurements during and postshaking.

Even though the drag and pile tip loads decreased during shaking, the piles suffered large settlements [Fig. 8(b)]. High excess pore pressures generated around the pile decreased the pile's shaft and tip capacity and its stiffness resulting in penetration of pile in the soil until enough resistance was mobilized to achieve force equilibrium [Fig. 8(b)]. For the 0DPile, liquefaction occurred below the initial static neutral plane while also developing very high excess pore pressures at the pile's tip, which resulted in significant settlement during shaking [Fig. 8(b)]. During EQM_5 shaking event, the development of excess pore pressure ratio of $r_u = 0.9$ near the tip of the 0DPile (with a pile head load of 1,000 kN) made the pile unstable, causing plunging of the pile in soil by about 107 mm into the soil (Table 4). On the other hand, for the deeply embedded 5DPile with larger tip capacity and liquefaction occurring above the initial neutral plane, the pile still suffered some settlement, although small (<10 mm), due to some excess pore pressures generated in the soil around the shaft and near the tip below the initial static neutral plane (Table 4). Overall, the piles suffered significant settlements during all large shaking events due to their reduced shaft and tip capacities and their stiffness from the excess pore pressures generated in the soil surrounding the pile.

Postshaking

At the end of shaking, excess pore pressures started dissipating, and consequently, the soil started reconsolidating. However, the presence of the low permeability clay layer (with effective stress of $\sigma'_{vo} = 38$ kPa at its bottom) hindered the drainage of water from the soil surface, leading to an equalization of excess pore pressures in the layers beneath near $u_e = 38$ kPa at $t \approx 2.5$ min [Figs. 6(a and b)]. The hindrance of drainage led to a water film formation beneath the clay-sand interface (also observed in other tests with impermeable interfaces, e.g., Malvick et al. 2002). The surface settlement remained almost constant during this period, with small, probably localized, heaving as shown in Figs. 6(a and b). The heaving must have resulted from the redistribution of the water film (Fiegel and Kutter 1994), which eventually drained through leakage from cracks in the clay layer and along the sides of the centrifuge model container. At about $t = 8$ min, the water film layer had fully disappeared. During this period ($t = 2.5$–8 min), the model surface settled by about 45 mm at a constant excess pore pressure of $u_e \approx 34$ kPa and $r_u = 52\%$ [Fig. 8(a)]. Once the water film fully dissipated ($t > 8$ min), excess pore pressure in the soil started to dissipate faster from gaps created in the clay layer or from the sides of the container [Figs. 6(a and b)]. Video recordings showed water coming to the surface along the sides of the container. Full reconsolidation (>98%) was achieved within 45–60 min. At the end of full reconsolidation, the settlement in the soil was measured to be about 65 mm (i.e., about 0.7% of volumetric strain) [Fig. 8(a)].

During reconsolidation, as excess pore pressures dissipated and the soil settled, the negative skin friction and hence the drag loads increased on the piles [Figs. 8(a and c)]. The decrease in excess pore pressure and correspondingly increase in drag load at $t =$ 1 min, $t = 5$ min, and $t = 1$ h is shown in Fig. 7(c). Between $t =$ 0.5–2.5 min, while the surface did not settle [Figs. 6(a) and 8(a)], the negative skin friction in the reconsolidating liquefied layer kept on increasing [Fig. 8(c)]. The increase in negative skin friction can be explained by the reconsolidation (dissipation of excess pore pressures by about 45%) occurring within the liquefied layer; however, it did not show up as the surface settlement because the water expelled in this process produced the water film layer under the clay. Consequently, the load at the shaft and the tip below the neutral plane also increased [Figs. 7(b and c) and Figs. 8(c and d)]. However, the resulting pile settlement was smaller as the piles regained their tip capacity and stiffness [Fig. 8(b)]. During reconsolidation,

Table 4. Summary of soil and pile settlement for all the shaking events at $t = 30$ s (end of shaking), $t = 2.5$ min, and at the end of reconsolidation

	0DPile			5DPile			Soil		
Event	$t = 30$ s	$t = 2.5$ min	Final[a]	$t = 30$ s	$t = 2.5$ min	Final[a]	$t = 30$ s	$t = 2.5$ min	Final[a]
EQM_1	0	0	0	0	0	0	2	2	3
EQM_2	6	6	6	3	3	3	14	15	20
EQM_3	10	12	12	1	2	3	13	24	70
EQM_4	4	5	5	1	2	2	12	13	17
EQM_5	114	120	123	2	3	4	14	17	71
EQM_6	54[b]	57	60	7	8	9	19	28	72

[a]After complete reconsolidation.
[b]For EQM_6 the duration of shaking was about 70 s.

settlements in the piles were less than 10 mm (i.e., 1.6% of pile diameter) (Table 4).

After complete reconsolidation ($r_u = 0$), the achieved drag load was higher than the initial drag load before shaking, while the neutral plane depths remained unchanged [Figs. 7(b and c) and 8(c)]. The increase in drag load resulted from the increased mobilized negative skin friction [Fig. 8(c)] above the neutral plane, which was caused either by (1) the increased soil displacement at the interface or (2) the increased lateral stresses from densification. For the 5DPile, the negative interface skin friction in the liquefiable layer increased from −20 to −40 kPa [Fig. 8(c)]. Ganainy et al. (2014) and Kokkali et al. (2018) used tactile pressure sensors in centrifuge model tests and observed the lateral stresses after reconsolidation higher than their initial value before shaking. After complete reconsolidation, the drag load on the 0DPile and 5DPile for shaking event EQM_3 increased from 250 to 500 kN and from 700 to 1,100 kN, respectively [Figs. 7(b and c)]. Consequently, the mobilized tip stress (and tip load) in the 0DPile and 5DPile increased from 1.5 to 2.2 MPa and from 2.2 to 3.0 MPa, respectively [Fig. 8(d)].

Discussion on Drag Loads

With multiple shakings, the magnitude of drag load was observed to increase in these centrifuge tests. For each shaking event, the drag load on the piles first decreased during shaking and increased during reconsolidation, eventually exceeding the value before shaking [Figs. 7(b and c)]. the pile head load (Q_f), load at the neutral plane (Q_{np}), drag load (Q_d), and tip load (Q_{tip}) for 0DPile and 5DPile after each shaking event and centrifuge spin-up are summarized in Fig. 9. The axial load profiles in piles after each shaking event are shown in Figs. 10(a and b). It can be seen from the figures that while the initial static neutral plane depth in the piles remained almost the same across all shaking events [Figs. 10(a and b)], the drag loads kept on increasing (Fig. 9). Shaking events (EQM_1, EQM_2, and EQM_3) after Spin-Up 1 resulted in the increase of drag loads from 250 to 500 kN in the 0DPile and from about 700 to 1,100 kN in the 5DPile. The increase in drag load also increased the load at the tip (Figs. 9 and 10). This increase in drag load could be due to the gradual increase of the effective lateral stress during reconsolidation. It remains to be confirmed whether the increase in lateral stress is due to dilatancy of the soil adjacent to the pile producing increased lateral stresses locally around the pile or an artifact of the centrifuge model container flexibility. Another possible mechanism could be the increased stiffness of tip (due to soil stronger or increase in embedment from pile settlement) in each successive event resulting in small downdrag settlement and larger drag load. The mechanism of the increase of drag loads with successive shaking events should continue to be investigated. Shaking events (EQM_4, EQM_5, and EQM_6) after Spin-Up 2 also increased drag loads in the piles. It increased from 150 to 500 kN in the 0DPile and from about 700 to 1,100 kN in the 5DPile. However, for the 5DPile, the drag load and the axial load distribution for shaking events EQM_5 and EQM_6 remained almost the same (Figs. 9 and 10). The drag load for the 5DPile may have achieved saturation at about 1,100 kN, which could have resulted from the full mobilization of interface skin friction and stabilization of lateral stresses.

Centrifuge spin-down and spin-up changed drag load on the piles. At the end of shaking event EQM_3, the centrifuge was stopped, and the pile head mass for the 0DPile was increased (from 500 kN to 1,000 kN). The model was then left overnight, causing the soil to rebound at 1 g. The next day after spinning up the centrifuge (Spin-Up 2), the developed drag loads on both piles were found less than they were after the shaking event EQM_3. The neutral plane depth developed at the same depth as before. The decrease in drag load from centrifuge spin-down and spin-up can be explained by changes in the lateral stresses caused by stopping and starting the centrifuge. As may be expected, for the 0DPile, the increase in pile head load from 500 to 1,000 kN resulted in developing smaller drag loads during Spin-Up 2 than during Spin-Up 1. The drag load developed in the 0DPile after Spin-Up 2 was about 150 kN compared to 250 kN after Spin-Up 1. On the other hand, the 5DPile (with no head load changed), after Spin-Up 2, developed the same drag load equal to 700 kN achieved after Spin-Up 1.

While estimating the exact lateral stresses developed at the interface is difficult, the results suggest that liquefaction-induced downdrag can mobilize negative skin friction equal to the interface shear strength. A conceptual limit load curve (indicated by dashed continuous lines) was found to envelop the pile's axial load profiles. The limit load curve is defined as the axial load distribution of the pile corresponding to the maximum drag load the pile can develop. Assuming the pile mobilizes negative skin friction equal to its interface shear strength, the maximum drag load was estimated. The limit load curve was obtained by assuming full mobilization of the interface shear strength using the α method of AASHTO (2020) with an undrained shear strength (s_u) of 20 kPa and $\tau = K\sigma_v' \tan(\delta)$ in the loose sand layer with an interface friction angle of $\delta = 30°$ and lateral stress coefficient $K = 1$.

The development of negative skin friction requires small relative movements (about 5 mm) between the soil and pile (Rituraj and Rajesh 2022). The medium shaking events (EQM_2 and EQM_4), even though they did not fully liquefy the loose sand layer ($r_u \approx 50\%$), resulted in the development of negative skin friction and thus drag load on piles (Figs. 9 and 10). However, the increase in the drag load was smaller in magnitude compared to the large shaking events (EQM_3, EQM_5, and EQM_6) (Fig. 9). The free-field soil settlement and pile settlement caused by the medium shaking events was recorded to be about 20 and 5 mm, respectively. The relative soil settlement of 15 mm corresponds to about 2% of the pile diameter. Fleming et al. (2008) suggested displacements of 0.5%–2% of the pile's diameter to fully mobilize skin friction. Results from pile load tests, particularly on drilled shafts (of diameter < 2 m), show that the skin friction is fully mobilized at a relatively small displacement (in the order of 10–30 mm), depending on the soil's D_R (O'Neill 2001). These results show that even when the soil layers do not fully liquefy, settlements caused by the dissipation of excess pore pressures exceeding a small percentage of the pile diameter would be enough to mobilize large negative skin friction in a pile. Viewed another way, the 15 mm of relative soil settlement corresponds to a displacement equal to about two times the median grain diameter (D_{50}) of sand used in the centrifuge test. DeJong and Westgate (2009) and Martinez and Frost (2017) suggested an interface shear band thickness of 5–7 particle diameters adjacent to the interface. Assuming that the elastic settlement in the shear band with respect to the free field soil settlement is small, a displacement of 2.0 D_{50} would produce a shear strain of 40% (assuming a shear band thickness of 5 D_{50}) which would likely be enough to mobilize the significant negative skin friction at the pile's interface.

Discussion on Pile Settlement

Most of the settlements in the piles occurred during shaking when the excess pore pressures around the pile's shaft and tip were high. On the other hand, the pile settlement (or downdrag settlement) during reconsolidation from liquefaction-induced downdrag was typically small (<2% of the pile's diameter). Pile settlement from all shaking events (Table 4) shows that pile settlements mainly occurred during shaking. The main cause for the large settlement of the piles was the decrease in pile tip capacity and stiffness from

increased excess pore pressures near the tip. Centrifuge tests showed that even if the bearing layer (in which the pile tip is embedded) is nonliquefiable, redistribution of excess pore pressures from the nearby liquefied layers and the generated earthquake-induced excess pore pressures can cause large excess pore pressure in the bearing layer. These large excess pore pressure near the tip significantly reduced the tip capacity and caused settlement in the piles. With the increase in the intensity of the shaking events, the free-field excess pore pressures developed near the pile's tip increased, and correspondingly the pile settlement also increased. For each successive shaking event EQM_1, EQM_2, EQM_3, EQM_5, and EQM_6, the free-field excess pore pressure ratio (r_u) at the 0DPile and 5DPile tip increased. This increased excess pore pressure caused an increase in pile settlements (Table 4). During the shaking events, EQM_5 and EQM_6, the 0DPile even plunged due to the development of very high excess pore pressure near its tip. During reconsolidation, while the drag loads increased, the shaft and tip capacity and stiffness (below the neutral plane) also increased, producing small pile settlements. As a result, for every event (except for 5DPile for small shaking events), the pile settlement during reconsolidation was much smaller (less than 10 mm, i.e., 0.16% of pile diameter) than the settlement caused during shaking (Table 4). The drag loads during reconsolidation thus had a tiny contribution (<2% of pile diameter) to the overall settlement of the pile.

Centrifuge test results show that the pile settlement during shaking governs the pile's performance. Furthermore, results also show that the magnitude of pile settlement is generally smaller than the free field settlement except for the large shaking events where the pile plunges due to the significant reduction of tip capacity from the migration of large excess pore pressures to the bearing layer. This differential settlement between the free-field and pile settlement can affect the postearthquake functionality of the structures. In some cases, especially where settlements are of the order of centimeters, settlement of piles similar to free-field soil settlements may improve postearthquake functionality of the superstructure (for example, in bridges). It is possible that if free-field settlement is, for example, 100 mm and the pile settlement is 50 mm, the bridge could be functional. However, the bridge would be closed if the pile settlement was zero—due to the 100-mm differential settlement between the bridge and the approach slab. Thus, differential settlement criteria should also be used in the design along with the absolute settlement criteria.

Summary and Conclusions

A large centrifuge model test was designed and performed to study liquefaction-induced downdrag on piles in a layered soil deposit. The soil profile included a loose liquefiable sand layer (9 m, $D_R = 42\%$) sandwiched between an impermeable clay crust (4 m) at the top and a dense nonliquefiable sand layer (8 m, $D_R = 86\%$) at the bottom. The clay crust was overlain with a 1-m-thick coarse sand ($D_R = 95\%$) layer with the water table at the ground surface. Two heavily instrumented piles of outer diameter 16 mm (model scale) were designed to represent a pipe pile of outer diameter 635 mm (prototype scale). Nine strain gauge bridges were installed inside the piles to measure the axial load distribution along the length of the piles. The piles were made sufficiently rough to achieve the maximum interface shear strength. The 0DPile and 5DPile were installed with their tips embedded zero times and five times their diameter in the dense sand layer, respectively. A lumped mass was clamped at the pile head. The model was shaken with six earthquake motions with peak ground accelerations ranging from 0.025 to 0.4 g, and the developed downdrag was monitored.

Some interesting pore pressure dissipation patterns were observed due to the soil layering consisting of sand and clay layers. During reconsolidation, the excess pore pressure quickly equalized within the sand layer. However, the overlying impermeable clay layer hindered the drainage and led to the formation of a water film beneath it. At this state, excess pore pressures in the soil at all depths "equalized" at a value equal to the effective stress beneath the clay layer. Ultimately, the water film dissipated, and excess pore pressures returned to zero within the next 45–60 min.

Some of the main findings from the experiment that should be accounted for in pile design are as follows:

- Soil settlements relative to the pile, of the order of 1%–2% of the pile diameter, are sufficient to mobilize significant negative skin friction.
- Complete liquefaction ($u_e = \sigma'_v$, $r_u = 1.0$) is not a prerequisite to the development of significant drag loads. Significant drag loads were observed for shaking events that produced excess pore pressures as low as 50% of the initial effective stress (i.e., $r_u \approx 0.5$). Results showed that after reconsolidation, the developed negative skin friction could equal the interface shear strength [$\tau = K\sigma'_v \tan(\delta)$] for both the nonliquefied ($r_u < 1.0$) as well as liquefied soils ($r_u = 1.0$). This is indifferent to the results from blast-induced liquefaction studies by Rollins and Strand (2006). They observed the magnitude of the negative skin friction in the reconsolidated liquefied (i.e., $r_u = 1.0$) layer as only 50% of the positive skin friction before shaking. The difference in the magnitude of negative skin friction in the reconsolidated liquefied layer may have been influenced by conditions not represented in these centrifuge tests.
- During shaking, excess pore pressures generated in the liquefiable layer reduced the negative skin friction, decreasing the drag loads and ultimately diminishing it to zero at complete liquefaction ($u_e \approx \sigma'_v$). However, as pore pressures dissipated, the drag loads again increased, approaching or surpassing the drag load that existed before shaking. Even though the neutral plane depth did not change at the end of shaking events, the gradual increase in lateral stresses and relative movement of soil at the pile's interface resulted in the higher mobilization of negative skin friction and drag load.
- Most of the pile settlement occurred during shaking when the excess pore pressures in the soil around the pile resulted in the loss of shaft and tip capacity and their stiffness. As such, the 5DPile embedded deep into the dense sand layer suffered tiny settlements throughout all shaking events. On the other hand, the 0DPile embedded barely in the dense sand layer suffered significant settlements in each shaking event. Comparatively, the postshaking settlement of the piles was small (<2% of pile diameter). For design, it would be recommended to check the settlement of piles for both the scenarios: (1) for the generated inertial loads during shaking with the reduced shaft and tip resistance from the excess pore pressures present near the shaft and the tip even if full liquefaction does not occur (i.e., $0 < r_u < 1$), and (2) from the development of drag load following soil reconsolidation combined with applicable structural loads. Furthermore, since most of the pile settlement occurs during shaking, if feasible, piles can be embedded deep into the bearing layer and thus maximizing their resistance and minimizing their settlement during shaking. Therefore, compared to liquefaction mitigation strategies, increasing the embedment of the pile could provide a cost-effective strategy to reduce pile settlements.
- Pile settlements are generally smaller than the free-field soil settlement if the tip capacity does not significantly decrease due to increased pore pressures near the pile's tip in the bearing layer. The differential settlement between the free-field and pile

settlement can affect the functionality of the superstructure (such as bridges). For example, a large differential settlement can create a gap between the bridge and the approaching slab, making the bridge unfunctional. It is thus suggested that there should be separate serviceability criteria for total pile settlement and differential settlement.

The test and data presented in this paper illuminated the mechanics of liquefaction-induced downdrag on piles through a simplified soil profile and allowed for some important conclusions to be made about how the various processes in these problems interact and affect each other. However, additional testing is required to thoroughly investigate downdrag phenomena for different soil profiles, different pile properties, and different shaking sequences.

Data Availability Statement

Some or all data, models, or code generated or used during the study are available in a repository online in accordance with funder data retention policies. All data used in this study are made available through DesignSafe under project PRJ-2828.

Acknowledgments

This work was funded by the California Department of Transportation under Agreement 65A0688. The authors would like to acknowledge Caltrans engineers and staff involved in this project for their suggestions and assistance. The authors thank the staff of the UC Davis Center for Geotechnical Modeling for making these experiments possible.

References

AASHTO. 2020. *AASHTO LRFD bridge design specifications*. LRFDUS-9. Washington, DC: AASHTO.

Bastidas, A. M. P. 2016. "Ottawa F-65 sand characterization." Ph.D. dissertation, Dept. of Civil and Environmental Engineering, Univ. of California, Davis.

Boulanger, R. W., and S. J. Brandenberg. 2004. "Neutral plane solution for liquefaction-induced down-drag on vertical piles." In *Geotechnical engineering for transportation projects*, 470–478. Reston, VA: ASCE. https://doi.org/10.1061/40744(154)32.

Carey, T. J., N. Stone, and B. L. Kutter. 2020. "Grain size analysis and maximum and minimum dry density of Ottawa F-65 Sand for LEAP-UCD-2017." In *Model tests and numerical simulations of liquefaction and lateral spreading*, edited by B. L. Kutter, M. T. Manzari, and M. Zeghal, 31–44. Cham, Switzerland: Springer. https://doi.org/10.1007/978-3-030-22818-7_2.

Coelho, P. A. L. F., S. K. Haigh, S. P. G. Madabhushi, and T. O'Brien. 2004. "Centrifuge modelling of the use of densification as a liquefaction resistance measure for bridge foundations." In *Proc., 13th World Conf. on Earthquake Engineering, Paper No. 210*. Vancouver, BC, Canada: Canadian Association for Earthquake Engineering.

DeJong, J. T., and Z. J. Westgate. 2009. "Role of initial state, material properties, and confinement condition on local and global soil-structure interface behavior." *J. Geotech. Geoenviron. Eng.* 135 (11): 1646–1660. https://doi.org/10.1061/(ASCE)1090-0241(2009)135:11(1646.

Elvis, I. 2018. "Liquefaction-induced dragload and/or downdrag on deep foundations within the New Madrid seismic zone." Ph.D. dissertation, Dept. of Civil Engineering, Univ. of Arkansas.

Fellenius, B. H. 2004. "Unified design of piled foundations with emphasis on settlement analysis." In *Current practices and future trends in deep foundations*, 253–275. Reston, VA: ASCE. https://doi.org/10.1061/40743(142)15.

Fellenius, B. H. 2006. *Basics of foundation design*. Sidney, BC: Electronic Edition.

Fellenius, B. H., B. Abbasi, and B. Muhunthan. 2020. "Liquefaction induced downdrag for the Juan Pablo II Bridge at the 2010 Maule Earthquake in Chile." *Geotech. Eng. J.* 51 (2): 1–8.

Fellenius, B. H., and T. C. Siegel. 2008. "Pile drag load and downdrag in a liquefaction event." *J. Geotech. Geoenviron. Eng.* 134 (9): 1412–1416. https://doi.org/10.1061/(ASCE)1090-0241(2008)134:9(1412.

Fiegel, B. G. L., and B. L. Kutter. 1994. "Liquefaction mechanism for layered sands." *J. Geotech. Eng.* 120 (4): 737–755. https://doi.org/10.1061/(ASCE)0733-9410(1994)120:4(737.

Fleming, K., A. Weltman, M. Randolph, and K. Elson. 2008. *Piling engineering*. London: CRC Press. https://doi.org/10.1201/b22272.

Ganainy, H., A. El Tessari, T. Abdoun, and I. Sasanakul. 2014. "Tactile pressure sensors in centrifuge testing." *Geotech. Test. J.* 37 (1): 151–163. https://doi.org/10.1520/GTJ20120061.

Garnier, J., C. Gaudin, S. M. Springman, P. J. Culligan, D. Goodings, D. Konig, B. Kutter, R. Phillips, M. F. Randolph, and L. Thorel. 2007. "Catalogue of scaling laws and similitude questions in geotechnical centrifuge modelling." *Int. J. Phys. Model. Geotech.* 7 (3): 1–23. https://doi.org/10.1680/ijpmg.2007.070301.

Hannigan, P. J., F. Rausche, G. E. Likins, B. R. Robinson, and M. L. Becker. 2016. *Design and construction of driven pile foundations*. FHWA-NHI-16-009. Woodbury, MN: Federal Highway Administration.

Ilankatharan, M. 2008. "Centrifuge modeling for soil-pile-bridge systems with numerical simulations accounting for soil-container-shaker interaction." Ph.D. dissertation, Dept. of Civil and Environmental Engineering, Univ. of California, Davis.

Knappett, J. A., and S. P. G. Madabhushi. 2009. "Seismic bearing capacity of piles in liquefiable soils." *Soils Found.* 49 (4): 525–535. https://doi.org/10.3208/sandf.49.525.

Kokkali, P., T. Abdoun, and M. Zeghal. 2018. "Physical modeling of soil liquefaction: Overview of LEAP production test 1 at Rensselaer Polytechnic Institute." *Soil Dyn. Earthquake Eng.* 113 (Oct): 629–649. https://doi.org/10.1016/j.soildyn.2017.01.036.

Lusvardi, C. M. 2020. "Blast-induced liquefaction and downdrag development on a micropile foundation." Ph.D. dissertation, Dept. of Civil and Environmental Engineering, Brigham Young Univ.

Malvick, E. J., R. Kulasingam, R. W. Boulanger, and B. L. Kutter. 2002. *Effects of void redistribution on liquefaction flow of layered soil—Centrifuge data report for EJM01*. UCD/CGMDR-02/02. Davis, CA: Univ. of California, Davis.

Martinez, A., and J. D. Frost. 2017. "The influence of surface roughness form on the strength of sand–structure interfaces." *Geotech. Lett.* 7 (1): 104–111. https://doi.org/10.1680/jgele.16.00169.

Muhunthan, B., N. V. Vijayathasan, and B. Abbasi. 2017. *Liquefaction-induced downdrag on drilled shafts*. WA-RD 865.1. Pullman, WA: Washington State DOT.

Nicks, J. 2017. *Liquefaction-induced downdrag on Continuous Flight Auger (CFA) piles from full-scale tests using blast liquefaction*. FHWA-HRT-17-060. McLean, VA: Federal Highway Administration.

O'Neill, M. W. 2001. "Side resistance in piles and drilled shafts." *J. Geotech. Geoenviron. Eng.* 127 (1): 3–16. https://doi.org/10.1061/(ASCE)1090-0241(2001)127:1(3.

Rituraj, S. S., and B. G. Rajesh. 2022. "Negative skin friction on piles: State of the art." In *Advances in geo-science and geo-structures, lecture notes in civil engineering*, edited by A. K. Choudhary, S. Mondal, S. Metya, and G. L. S. Babu, 323–335. Singapore: Springer. https://doi.org/10.1007/978-981-16-1993-9_34.

Rollins, K. 2017. "Dragload and downdrag on piles from liquefaction induced ground settlement." In *Proc., US–New Zealand–Japan Int. Workshop on Liquefaction-Induced Ground Movement Effects*, edited by J. D. Bray, R. W. Boulanger, M. Cubrinovski, K. Tokimatsu, S. L. Kramer, T. O'Rourke, R. A. Green, P. K. Robertson, and C. Z. Beyzaei. Berkeley, CA: Univ. of California Berkeley.

Rollins, K., and J. Hollenbaugh. 2015. "Liquefaction induced negative skin friction from blast-induced liquefaction tests with auger-cast piles." In *Proc., 6th Int. Conf. Earthquake Geotechnical Engineering*. Christchurch, New Zealand: International Society for Soil Mechanics and Geotechnical Engineering.

Rollins, K. M., C. Lusvardi, S. Amoroso, and M. Franceschini. 2019. "Liquefaction induced downdrag on full-scale micropile foundation."

In *Proc., 2nd Int. Conf. on Natural Hazards and Infrastructure*. Chania, Greece: Innovation Center for Natural Hazards and Infrastructure.
Rollins, K. M., and S. R. Strand. 2006. "Downdrag forces due to liquefaction surrounding a pile." In *Proc., 8th National Conf. Earthquake Engineering*. San Francisco: Earthquake Engineering Research Institute.
Rollins, K. M., and S. R. Strand. 2007. *Liquefaction mitigation using vertical composite drains: Full-scale testing for pile applications*. Washington, DC: Transportation Research Board.
Sinha, S. K. 2022. "Liquefaction-induced downdrag on piles: Centrifuge and numerical modeling, and design procedures." Ph.D. dissertation, Dept. of Civil and Environmental Engineering, Univ. of California, Davis.
Sinha, S. K., K. Ziotopoulou, and B. L. Kutter. 2019. "Parametric study of liquefaction induced downdrag on axially loaded piles." In *Proc., 7th lnt. Conf. on Earthquake Geotechnical Engineering*. Rome: International Society for Soil Mechanics and Geotechnical Engineering.
Sinha, S. K., K. Ziotopoulou, and B. L. Kutter. 2021. *Centrifuge testing of liquefaction-induced downdrag on axially loaded piles: Data report for SKS02*. UCD/CGMDR–21/01. Davis, CA: Univ. of California, Davis.
Strand, S. 2008. "Liquefaction mitigation using vertical composite drains and liquefaction-induced downdrag on piles: Implication for deep foundation design." Ph.D. dissertation, Dept. of Civil and Environmental Engineering, Brigham Young Univ.
Stringer, M. E., B. L. Kutter, D. W. Wilson, Y. G. Zhou, and B. L. Zheng. 2013. *Steel pile jacket seismic soil structure interaction study: Phase 2 data report*. UCD/CGMDR-12/02. Davis, CA: Univ. of California, Davis.
Stringer, M. E., and S. P. G. Madabhushi. 2010. "Effect of liquefaction on pile shaft friction capacity." In *Proc., 5th Int. Conf. on Recent Advances in Geotechnical Earthquake Engineering and Soil Dynamics*, edited by S. Prakash. San Diego: Missouri Univ. of Science and Technology.
Stringer, M. E., and S. P. G. Madabhushi. 2013. "Re-mobilization of pile shaft friction after an earthquake." *Can. Geotech. J.* 50 (9): 979–988. https://doi.org/10.1139/cgj-2012-0261.
Vijayaruban, V. N., B. Muhunthan, and B. H. Fellenius. 2015. "Liquefaction-induced downdrag on piles and drilled shafts." In *Proc., 6th Int. Conf. on Earthquake Geotechnical Engineering*. Christchurch, New Zealand: International Society for Soil Mechanics and Geotechnical Engineering.